

# Virtual finite element and hyperbolic problems: the PAMPA algorithm.

Remi Abgrall<sup>\*</sup>, Walter Boscheri<sup>†</sup>, and Yongle Liu<sup>\*</sup>

(<sup>\*</sup>) Institute of Mathematics, University of Zürich, Switzerland

(<sup>†</sup>) Laboratoire de MathA(C)matiques UMR 5127 CNRS, UniversitA(C) Savoie Mont Blanc, France

## Abstract

In this paper, we explore the use of the Virtual Element Method concepts to solve scalar and system hyperbolic problems on general polygonal grids. The new schemes stem from the active flux approach [1], which combines the usage of point values at the element boundaries with an additional degree of freedom representing the average of the solution within each control volume. Along the lines of the family of residual distribution schemes introduced in [2, 3] to bridge the active flux technique, we devise novel third order accurate methods that rely on the VEM technology to discretize gradients of the numerical solution by means of a polynomial-free approximation, hence adopting a virtual basis that is locally defined for each element. The obtained discretization is globally continuous, and for nonlinear problems it needs a stabilization which is provided by the *a posteriori* MOOD paradigm [4]. This is applied to both point and average values of the discrete solution. We show applications to scalar problems, as well as to the acoustics and Euler equations in 2D. The accuracy and the robustness of the proposed schemes are assessed against a suite of benchmarks involving smooth solutions, shock waves and other discontinuities.

## 1 Introduction

In [1, 5, 6], a new numerical method is introduced for solving hyperbolic problems on triangular unstructured meshes. The numerical solution is approximated employing the degrees of freedom (DoFs) of the quadratic polynomials, which are all lying on the boundary of the elements, supplemented by another degree of freedom: the average of the solution. This leads to a potentially third order accurate method, with an approximation that is globally continuous. The time integration relies on a back-tracing of characteristics. The extension of this scheme to square elements, in a finite difference fashion, has then been forwarded in [7, 8]. In [2], a different, though very close, point of view is proposed. The time marching algorithm relies on standard Runge-Kutta time stepping, and several versions of the same scheme can be used without preventing local conservation. These routes have been followed in [9], giving several versions of higher order approximations, in one space dimension. Later on, the problem of nonlinear stabilization has received attention: besides the MOOD technique already employed in [2] and other papers, a direct method is being considered, see [10, 11].

More recently, extensions to triangles have been developed in the spirit of [2] where the degrees of freedom are again given by Lagrange point values on the boundary of elements and one average in the element. Two cases have been dealt with: the “quadratic” case where the point value DoFs are the 6 Lagrange points, and the “cubic” case where we consider only the 9 Lagrange points that are on the boundary. In both cases, the approximation space, on each element  $P$  is generated by basis functions denoted as  $\{\varphi_\sigma\}$  for the DoFs on the boundary of  $P$  and  $\bar{\varphi}_P$  for the average value. These basis functions are such that:

- $\bar{\varphi}_P$  vanishes on  $\partial P$  and  $\int_P \bar{\varphi} d\mathbf{x} = 1$  (conservation property);
- For all  $\sigma$ ,  $\int_P \varphi_\sigma d\mathbf{x} = 0$  and  $\varphi_\sigma(\sigma') = \delta_\sigma^{\sigma'}$  (interpolation property);
- Finally,  $\bar{\varphi}$  and all the  $\varphi_\sigma$  are quadratic (for the first case) and cubic (for the second case) polynomials (accuracy property).

The space generated by these functions is denoted by  $V_P$ . By means of this approximation, we see that for a conformal mesh, the only "active" degrees of freedom on any face are those ones belonging to that face, and thus we see that  $V = \oplus_P V_P \subset C^0(\Omega)$  if  $\{P\}$  is a conformal triangulation of  $\Omega \subset \mathbb{R}^2$ . We have that  $\mathbb{P}^2 \subset V$  for the quadratic case (resp.  $\mathbb{P}^3 \subset V$  for the cubic case). It turns out that the three-dimensional case could be done in the same way because the dimension of  $\mathbb{P}^2$  is 10 and that of  $\mathbb{P}^3$  is 20. We have exactly the right amount of information to have unisolvance and to cover exactly  $\mathbb{P}^k$  for  $k = \{2, 3\}$ .

One may wonder, however, what is the interest of all this. Having a globally continuous approximation helps to reduce the number of degrees of freedom, compared for example to discontinuous Galerkin schemes, where the DoFs are doubled on all element boundaries (apart from the physical boundary of the computational domain). Looking at the method of [2], we see that we have the same kind of numerical stencil: this is good for the parallelization of the method. Nevertheless, the mesh must be conformal, so that mesh refinement, both  $h$  and  $p$ , is not an easy task. Thus, we want to develop a method that is very compact, allows for globally continuous approximation and is friendly to mesh refinement, both with  $h$  and  $p$  refinement. The bottleneck is that we had to use basis functions in the previous formulations, that are defined on standard (or reference) elements, namely the unit triangle or square in 2D (resp. the unit tetrahedron or cube in 3D). How to get rid of them?

Looking at the finite element literature, there are two possible tracks, both inspired from the mimetic approximations [12]: i) the Virtual Finite Element VEM method by Brezzi et al.[13, 14], ii) and the HHO schemes introduced by di Pietro, Droniou and co-authors[15]. In this paper, we will get inspiration from the VEM method where no basis functions are explicitly needed, arbitrary polygonal meshes can be adopted in 2D (polyhedral meshes in 3D), with globally continuous approximation. This allows mesh refinement without hanging nodes. We will recall these spaces in Appendix A. Note that, differently from the classical VEM framework, we only need the approximation properties of the VEM spaces, and no variational formulation is used, besides those used in [2] and [9].

This format of this paper is as follows. First, we recall the approximation spaces and how we construct the polygonal meshes. Then, we describe the schemes, the high order one and the low order one that we need for nonlinear stabilization. Finally, we present a set of numerical examples using triangle, quadrangle and general polygonal meshes, validating the accuracy and the robustness of the novel schemes. A conclusion follows.

## 2 Meshes and Approximation space

### 2.1 Meshes

Given  $\Omega \subset \mathbb{R}^2$  that is assumed to be polygonal, we first start by constructing a triangular mesh using GMSH [16]. GMSH can also consider quadrangular meshes. This is also doable in 3D. If we consider only triangular or quadrilateral meshes, we fit the formalism outlined in [2]. Otherwise, arbitrary polygonal meshes must be faced, and we consider the following options for generating the computational mesh.

1. The centroids, i.e. the barycenters, of the GMSH elements are connected with the mid points of the edges, hence obtaining a dual mesh with respect to the original one [17, 18].
2. A genuinely Voronoi mesh can be constructed from the vertices of the GMSH mesh by connecting the circumcenters of the GMSH elements which share a common vertex.
3. A more regular polygonal grid is built starting from the vertices of the GMSH mesh by connecting the barycenters of the GMSH elements which share a common vertex. This is no longer a Voronoi mesh, but typically it yields more regular hexagonal polygons [19].

In all cases, the physical boundary of the domain is preserved, thus the polygonal boundary elements are modified accordingly. Option 3 is mostly adopted in this paper, because it leads to a higher quality of the element shape, and our numerical method does not need any orthogonality property which would otherwise imply the usage of a Voronoi grid *sensu stricto* [20].

## 2.2 Approximation space

The approximation space is the same of the one adopted by the Virtual Finite Element Method (VEM) [13]. We first introduce some notations, following closely [13]. The computational domain  $\Omega$  is covered by a set of non-empty and non-overlapping polygons that are denoted by  $P$ . The notation  $\mathbf{x}_P$  represents the centroid of  $P$ . The elements  $P$  may not be convex, but they are assumed to be star-shaped with respect to a point  $\mathbf{y}_P$  (that may be different of  $\mathbf{x}_P$ ). For  $D \subset \Omega$ , the  $L^2$  inner product between two functions in  $L^2(D)$  is  $\langle u, v \rangle_D$ . When there is no ambiguity on  $D$ , we omit the subscript  $D$ . For  $\boldsymbol{\alpha} = (\alpha_1, \alpha_2)$ , the scaled monomial of degree  $|\boldsymbol{\alpha}| = \alpha_1 + \alpha_2$  are defined by

$$m_{\boldsymbol{\alpha}} = \left( \frac{\mathbf{x} - \mathbf{x}_P}{h_P} \right)^{\boldsymbol{\alpha}} = \left( \frac{x - x_P}{h_P} \right)^{\alpha_1} \left( \frac{y - y_P}{h_P} \right)^{\alpha_2}, \quad \mathbf{x} = (x, y). \quad (1)$$

Here,  $h_P$  is the diameter of  $P^1$ , according to the definition given in [13]. The set of scaled monomials of degree  $|\boldsymbol{\alpha}| \leq k$  is a basis of  $\mathbb{P}_k(P)$ , which denotes the vector space of polynomials of degree less or equal to  $k$ , defined on  $P$ . Similar definitions and comments can be done in three space dimensions. The scaled monomials are invariant by homothety: if  $\hat{\mathbf{x}} = \lambda \mathbf{x}$ , then

$$\hat{m}(\hat{\mathbf{x}}) = \left( \frac{\hat{\mathbf{x}} - \mathbf{x}_{\hat{P}}}{h_{\hat{P}}} \right)^{\boldsymbol{\alpha}} = m_{\boldsymbol{\alpha}} = \left( \frac{\mathbf{x} - \mathbf{x}_P}{h_P} \right)^{\boldsymbol{\alpha}}, \quad (2)$$

because  $\hat{P}$  is the image of  $P$  by this mapping.

Now we introduce the degrees of freedom of the approximation space and define the local virtual space  $V_k(P)$  for each  $P$ . For  $k \geq 2$ , a function  $v_h \in V_k(P)$  is uniquely defined by the following setup:

1.  $v_h$  is a polynomial of degree  $k$  on each edge  $e$  of  $P$ , that is  $(v_h)|_e \in \mathbb{P}_k(e)$ ,
2.  $v_h$  is continuous on  $\partial P$ ,
3.  $\Delta v_h \in \mathbb{P}_{k-2}(P)$ .

The third condition has nothing to do with any PDE problem we could have in mind, we will comment later on its usefulness. Notice that  $\mathbb{P}_k(P) \subset V_k(P)$ , and a function of  $V_k(P)$  is uniquely defined by the degrees of freedom given by:

1. The value of  $v_h$  at the vertices of  $P$ ,
2. On each edge of  $P$ , the value of  $v_h$  at the  $k - 1$  internal points of the  $k + 1$  Gauss-Lobatto points on this edge,
3. The moments up to order  $k - 2$  of  $v_h$  in  $P$ ,

$$m_{\boldsymbol{\alpha}}(v_h) := \frac{1}{|P|} \int_P v_h m_{\boldsymbol{\alpha}} \, d\mathbf{x}, \quad |\boldsymbol{\alpha}| \leq k - 2. \quad (3)$$

The dimension of  $V_k(P)$  is

$$\dim V_k(P) = N_V \cdot k + \frac{k(k-1)}{2}, \quad (4)$$

with  $N_V$  representing the number of vertices of  $P$ . The total number of degrees of freedom are then referred to with  $N_{\text{DoFs}} := \dim V_k(P)$ . Let  $\{\varphi_i\}_{i=1}^{N_{\text{DoFs}}}$  be the canonical basis for  $V_k(P)$ . We can then represent each  $v_h \in V_k(P)$  in terms of its degrees of freedom by means of a Lagrange interpolation:

$$v_h = \sum_{i=1}^{N_{\text{DoFs}}} \text{DoF}_i(v_h) \varphi_i. \quad (5)$$

---

<sup>1</sup>Other choices are possible, such as a set of orthogonal polynomials [21]. This set should contain the constant function 1. This kind of choice allows for a better conditioning of the linear systems.

For this basis, the usual interpolation property holds true:

$$\text{DoF}_i(\varphi_j) = \delta_{ij}, \quad i, j = 1, \dots, N_{\text{DoFs}}. \quad (6)$$

The first step is to construct a projector  $\pi^\nabla$  from  $V_k(P)$  onto  $\mathbb{P}_k(P)$ . It is defined by two sets of properties. First, for any  $v_h \in V_k(P)$ , the orthogonality condition

$$\langle \nabla p_k, \nabla(\pi^\nabla v_h - v_h) \rangle = 0, \quad \forall p_k \in P_k(P), \quad (7)$$

has to hold true, which is defined up to the projection onto constants  $P_0 : V_k(P) \rightarrow \mathbb{P}_0(P)$ , that can be fixed as follows:

- if  $k = 1$ ,

$$P_0(v_h) = \frac{1}{N_V} \sum_{i=1}^{N_V} v_h(\mathbf{x}_i), \quad (8)$$

- if  $k \geq 2$ ,

$$P_0(v_h) = \frac{1}{|P|} \int_P v_h \, d\mathbf{x} = m_{(00)}(v_h). \quad (9)$$

Then, we ask that

$$P_0(\pi^\nabla v_h - v_h) = 0. \quad (10)$$

We can *explicitly* compute the projector by using only the degrees of freedom previously introduced: using the third condition of the definition of  $V(P)$ , it can be seen that

$$\int_P \nabla p_k \nabla v_h \, d\mathbf{x} = - \int_P \Delta p_k v_h \, d\mathbf{x} + \int_{\partial P} \nabla v_k \cdot \mathbf{n} v_h \, d\gamma$$

so that  $\int_P \nabla p_k \nabla v_h \, d\mathbf{x}$  is computable from the degrees of freedom only. Since  $\pi^\nabla v_h \in \mathbb{P}_k(P)$ , we can find  $\dim \mathbb{P}_k(P) = \frac{k(k+1)}{2}$  real numbers  $s_\alpha$  such that

$$\pi^\nabla v_h = \sum_{|\alpha|=1}^{\dim \mathbb{P}_k(P)} s_\alpha m_\alpha, \quad (11)$$

and then

$$P_0(\pi^\nabla v_h) = \sum_{\alpha, |\alpha| \leq k} s_\alpha \cdot P_0(m_\alpha) = P_0(v_h). \quad (12)$$

Integration by parts yields

$$\sum_{\alpha, |\alpha| \leq k} s_\alpha \langle \nabla m_\alpha, \nabla m_\beta \rangle = \int_P \nabla m_\beta \nabla v_h \, d\mathbf{x} = - \int_P \Delta m_\beta v_h \, d\mathbf{x} + \int_{\partial P} v_h \nabla m_\beta \cdot \mathbf{n} \, d\gamma, \quad (13)$$

and since  $\Delta m_\beta \in \mathbb{P}_{k-2}(P)$ , one can find a family of real coefficients  $d_\delta(m_\beta)$  such that

$$\Delta m_\beta = \sum_{\delta, |\delta| \leq k-2} d_\delta(m_\beta) m_\delta,$$

the volume integral defined above can be computed by

$$\int_P v_h \Delta m_\beta \, d\mathbf{x} = \sum_{\delta, |\delta| \leq k-2} d_\delta(m_\beta) \int_P m_\delta v_h \, d\mathbf{x} = |P| \sum_{\delta, |\delta| \leq k-2} d_\delta(m_\beta) m_\delta(v_h). \quad (14)$$

Similarly,  $\int_{\partial P} \nabla m_\beta \cdot \mathbf{n} v_h d\gamma$  is computable because  $v_h$  is a polynomial of degree  $k$  on  $\partial P$ . Note that, since the point values at the Gauss-Lobatto points are known, no additional computation is needed.

By gathering the information contained in (12) and (14), we obtain a linear system

$$G_P \cdot \mathbf{s} = \mathbf{c}$$

with  $\mathbf{s}$  the vector of components  $s_\alpha$  and  $\mathbf{c}$  the vector of components

$$c_\alpha = - \int_P \nabla m_\alpha v_k d\mathbf{x} + \int_{\partial P} \nabla m_\beta \cdot \mathbf{n} v_h d\gamma.$$

The matrix  $G$  is

$$G = \begin{pmatrix} A \\ B \end{pmatrix},$$

where  $A$  is the vector containing the coefficients  $P_0(m_\alpha)$  for  $|\alpha| \leq k$  and  $B$  is the  $k \times (k-1)$  ‘‘mass matrix’’

$$B = (\langle \nabla m_\alpha, \nabla m_\beta \rangle)_{0 < |\alpha|, |\beta| \leq k}.$$

It is invertible because from (7) its kernel contains constant polynomials only, and from (10) this can be only 0.

### 3 Numerical schemes

The mathematical model is given by

$$\frac{\partial \mathbf{u}}{\partial t} + \operatorname{div} \mathbf{f}(\mathbf{u}) = 0, \quad (15)$$

where  $\mathbf{u} \in \mathcal{D} \subset \mathbb{R}^m$  is the vector of conserved variables,  $\mathcal{D}$  is the domain where  $\mathbf{u}$  is defined and  $\mathbf{f} = (f_1, \dots, f_d)$  is the flux tensor. The functions  $f_j$  for every  $j = 1, \dots, d$  are assumed to be defined and  $C^1$  on  $\mathcal{D}$ . This system, at least for smooth solutions, can be rewritten in a non-conservative form as

$$\frac{\partial \mathbf{u}}{\partial t} + \mathbf{A} \cdot \nabla \mathbf{u} = 0, \quad (16)$$

with the notation

$$\mathbf{A} \cdot \nabla \mathbf{u} = \sum_{j=1}^d A_j \frac{\partial \mathbf{u}}{\partial x_j} \text{ with } A_j = \frac{\partial f_j}{\partial \mathbf{u}}.$$

The governing equations are assumed to be hyperbolic, i.e. for any  $\mathbf{n} = (n_1, \dots, n_d) \in \mathbb{R}^d$ , the system matrix

$$\mathbf{A} \cdot \mathbf{n} = \sum_j A_j n_j$$

is diagonalisable in  $\mathbb{R}$ .

The canonical example of such a system is that of the Euler equations where, if  $\rho$  is the density,  $\mathbf{v}$  the velocity and  $E$  the total energy, we have  $\mathbf{u} = (\rho, \rho \mathbf{v}, E)^\top$ . The total energy is the sum of the internal energy  $e$  and of the kinetic energy  $\frac{1}{2} \rho \mathbf{v}^2$ . The invariant domain  $\mathcal{D}$  is

$$\mathcal{D} := \{\mathbf{u}, \text{ with } \rho \geq 0, e \geq 0\}.$$

The fluxes write

$$\mathbf{f}(\mathbf{u}) = \begin{pmatrix} \rho \mathbf{v} \\ \rho \mathbf{v} \otimes \mathbf{v} + p \operatorname{Id}_{d \times d} \\ (E + p) \mathbf{v} \end{pmatrix}$$

where we have introduced the pressure  $p = p(\rho, e)$ . In all the examples, the system is closed by the perfect gas equation of state, that is  $p = (\gamma - 1)e$ , where the ratio of specific heats  $\gamma$  is constant.

Other examples will be considered:

- A convection scalar problem where  $u \in \mathbb{R}$  and

$$\frac{\partial u}{\partial t} + \operatorname{div}(\mathbf{a} u) = 0,$$

with the advection speed  $\mathbf{a}$  possibly depending on the spatial coordinate.

- A nonlinear example

$$\frac{\partial u}{\partial t} + \frac{\partial(\sin u)}{\partial x} + \frac{\partial(\cos u)}{\partial y} = 0.$$

The time evolution will be carried out by mean of SSP Runge-Kutta schemes, so we only describe the first order forward Euler scheme.

### 3.1 High order schemes

On a generic polygon  $P$ , the numerical solution  $\mathbf{u}$  is represented by point values at the Gauss-Lobatto points of the edges of  $P$  and the average. The update of the average is simply done via

$$|P| \frac{d\bar{\mathbf{u}}}{dt} + \oint_{\partial P} \mathbf{f}(\mathbf{u}) \cdot \mathbf{n} \, d\mathbf{x} = 0. \quad (17)$$

On each edge  $e$  of  $P$ , we set

$$\oint_e \mathbf{f}(\mathbf{u}) \cdot \mathbf{n} = |e| \sum_{\sigma \in e} \omega_\sigma \mathbf{f}(\mathbf{u}_\sigma) \cdot \mathbf{n}, \quad (18)$$

where the  $\{\omega_\sigma\}$  are the weight of the Gauss-Lobatto points. Note that we have used the global continuity property of the approximation, and then no numerical flux is needed.

The update of the boundary values is more involved and we describe an extension of what have been proposed in several solutions. To update  $\mathbf{u}_\sigma$ , we consider a semi-discrete scheme of the form:

$$\frac{\partial \mathbf{u}_\sigma}{\partial t} + \sum_{P, \sigma \in P} \Phi_\sigma^P(\mathbf{u}^h) = 0 \quad (19)$$

where the quantities  $\Phi_\sigma^P(\mathbf{u}^h)$  are defined such that if the solution is linear and the problem linear with constant Jacobians, then we have

$$\sum_{P, \sigma \in P} \Phi_\sigma^P(\mathbf{u}^h) = \mathbf{A} \cdot \nabla \mathbf{u}(\sigma).$$

There is still a lot of freedom in the definition of  $\Phi_\sigma^P(\mathbf{u}^h)$ . Inspired by Residual Distribution schemes, and in particular looking at the LDA scheme [22], we consider

$$\Phi_\sigma^P = \mathbf{N}_\sigma K_\sigma^+ \left( \mathbf{A}(\mathbf{u}_\sigma) \cdot \nabla \pi_P^\nabla \mathbf{u}(\sigma) \right), \quad (20)$$

where

$$\mathbf{N}_\sigma^{-1} = \sum_{P, \sigma \in P} K_\sigma^+, \quad (21)$$

with the following definitions:

- $\mathbf{A}(\mathbf{u}_\sigma)$  is the Jacobian matrix evaluated for the state  $\mathbf{u}_\sigma$ ,
- For any  $\sigma \in P$ , we define a normal  $\mathbf{n}_\sigma$  as follows: For the polygon  $P$  and the DoFs  $\sigma$ , the vector  $\mathbf{n}_\sigma$  is the half sum of the normals of the faces  $e^+$  and  $e^-$  sharing  $\sigma$ . They may be identical, see Figure 1 for a definition of the  $e^\pm$  faces and normals  $\mathbf{n}^\pm$ ,

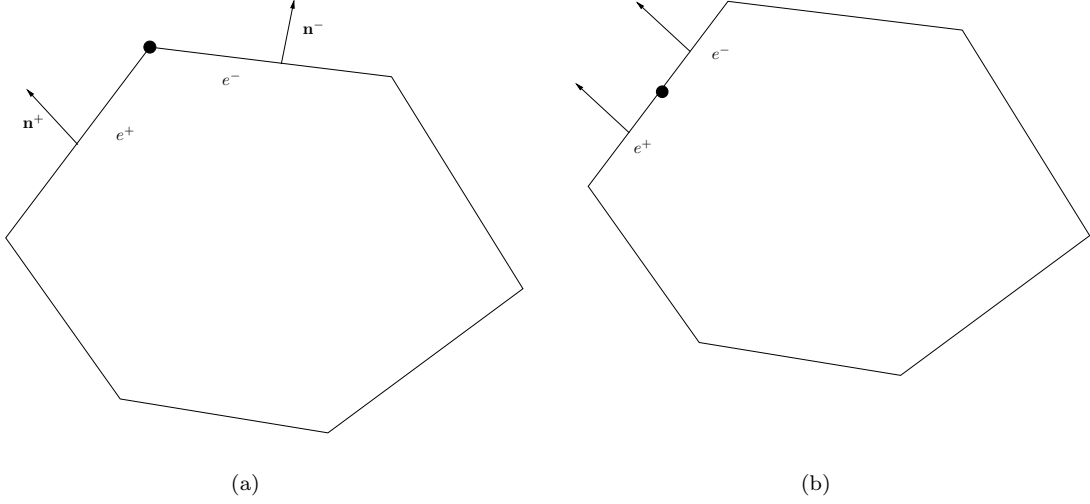


Figure 1: Definition of  $e^\pm$  and  $\mathbf{n}^\pm$ : (a) case of a vertex, (b) case of a non vertex.

- For any  $\mathbf{n}_\sigma = (n_x, n_y)$ ,  $K_\sigma := \mathbf{A}(\mathbf{u}_\sigma) \cdot \mathbf{n}_\sigma = A_x n_x + A_y n_y$  with  $A_x = \frac{\partial f_1}{\partial \mathbf{u}}$  and  $A_y = \frac{\partial f_2}{\partial \mathbf{u}}$ .
- Since the problem is hyperbolic, the matrix  $K_\sigma$  is diagonalisable in  $\mathbb{R}$ , and we can take its positive part

Assuming that  $\mathbf{u}$  is linear and the problem linear, we see that  $\pi^\nabla \mathbf{u}^h = \mathbf{u}^h$  because  $\mathbf{u}^h$  is linear and using the fact that  $\mathbf{A}$  does not depend on  $\mathbf{u}$ , we have

$$\begin{aligned}
 \sum_{P, \sigma \in P} \Phi_\sigma^P &= \sum_{P, \sigma \in P} \mathbf{N}_\sigma K_\sigma^+ (\mathbf{A} \cdot \nabla \pi_P^\nabla \mathbf{u}(\sigma)) \\
 &= \mathbf{N}_\sigma \left( \sum_{P, \sigma \in P} K_\sigma^+ \right) \mathbf{A} \cdot \nabla \mathbf{u}(\sigma) \\
 &= \mathbf{A} \cdot \nabla \mathbf{u}(\sigma),
 \end{aligned}$$

if the condition (21) is met. The only thing is to show that the matrix  $\sum_{P, \sigma \in P} K_\sigma^+$  is invertible. It turns out that this is true for a hyperbolic system that is symmetrizable. See [23] for a proof. For the sake of completeness, we reproduce the proof and give precise assumptions in Appendix B.

We can also define the matrix  $N$  from

$$\mathbf{N}^{-1} = \sum_{P, \sigma \in P} \text{sign } K_\sigma. \quad (22)$$

This defines a different scheme, that provides (qualitatively) the same results.

The scheme is formally third order accurate in space because

$$\sum_{P, \sigma \in P} \Phi_\sigma^P - \mathbf{A}(\mathbf{u}_\sigma) \cdot \nabla \mathbf{u}(\mathbf{u}_\sigma) = \sum_{P, \sigma \in P} \mathbf{N}_\sigma K_\sigma^+ \mathbf{A} \cdot [\nabla \pi_P^\nabla \mathbf{u}(\sigma) - \nabla \mathbf{u}(\sigma)],$$

so that for any matrix norm,

$$\left\| \sum_{P, \sigma \in P} \Phi_\sigma^P - \mathbf{A}(\mathbf{u}_\sigma) \cdot \nabla \mathbf{u}(\mathbf{u}_\sigma) \right\| \leq \sum_{P, \sigma \in P} \|\mathbf{N}_\sigma K_\sigma^+\| \|\nabla \pi_P^\nabla \mathbf{u}(\sigma) - \nabla \mathbf{u}(\sigma)\|,$$

and then

$$\sum_{P, \sigma \in P} \Phi_\sigma^P - \mathbf{A}(\mathbf{u}_\sigma) \cdot \nabla \mathbf{u}(\mathbf{u}_\sigma) = O(h^3).$$

It turns out that the scheme (19)-(20)-(21) is not fully satisfactory. Simulations on the vortex problem described in Section 4.2.3 show that spurious modes exist and are not damped. We interpret this as a loss of information while going from  $\mathbf{u}^h$  to  $\pi_P^\nabla \mathbf{u}^h$ : the dimension of  $V_k(P)$  is always larger than that of  $\mathbb{P}^k(P)$  for any  $P$  and any  $k$ . This is not true in the approximation described in [3] because we do not need any projector on triangular meshes. Because of that fact, we need to introduce some filtering. Again inspired by [13], we would like to add a term of the form

$$\int_P \nabla \mathbf{u} \cdot \nabla \varphi_\sigma \, d\mathbf{x},$$

which is approximated along the lines of [13] as

$$\mathcal{D}_\sigma = \alpha_P \sum_{r=1}^{N_{\text{DoFs}}} \text{DoF}_r(\mathbf{u} - \pi_P^\nabla \mathbf{u}) \text{DoF}_r(\varphi_\sigma - \pi_P^\nabla \varphi_\sigma), \quad (23)$$

where  $\alpha_P$  bounds the spectra radius of  $\mathbf{A}(\mathbf{u}) \cdot \mathbf{n}$  in  $P$ . We note that if the index  $r$  corresponds to the average, then for all  $\sigma$  on the boundary, we have

$$\int_P \varphi_\sigma \, d\mathbf{x} = \int_P \pi_P^\nabla \varphi_\sigma \, d\mathbf{x} = 0,$$

so that

$$\mathcal{D}_\sigma = \alpha_P \sum_{r=1, \text{not average}} \text{DoF}_r(\mathbf{u} - \pi_P^\nabla \mathbf{u}) \text{DoF}_r(\varphi_\sigma - \pi_P^\nabla \varphi_\sigma).$$

We also note that

$$\sum_{\sigma \in \partial P} \text{DoF}_\sigma(\mathbf{u}) = \sum_{r=1, \text{not average}} \text{DoF}_r(\mathbf{u} - \pi_P^\nabla \mathbf{u})^2 > 0,$$

if  $\mathbf{u}$  is not a polynomial. Let us notice that  $\mathcal{D}_\sigma = O(h^{k+1})$  so that the accuracy is kept.

### 3.2 Low order schemes

The update of the average value is carried out as follows:

$$\bar{\mathbf{u}}_P^{n+1} = \bar{\mathbf{u}}_P^n - \frac{\Delta t}{|P|} \sum_{e \text{ edge of } P} |e| \hat{\mathbf{f}}_{\mathbf{n}_e}(\bar{\mathbf{u}}_P^n, \bar{\mathbf{u}}_{P^-}^n), \quad (24)$$

where  $\mathbf{n}_e$  is the outward normal unit to the edge  $e$ , and  $P^-$  is the polygon sitting on the other side of  $e$ . If  $\hat{\mathbf{f}}$  is a monotone flux, then, the scheme will be stable. The main drawback of this approach is that there is no longer any coupling between the point values and the average values in the update (24). This might be a problem, but we have not found any concrete example where this approach fails.

Again, the update of the point values is a bit more subtle. For notations and graphical illustration, we refer to Figure 2. By assumption, there exists a point,  $\mathbf{x}^*$ , such that  $P$  is star-shaped with respect to this point. In practice, we have always taken the centroid, because all the polygons we have considered are convex. Then, as drawn in Figure 2, we connect this point to the degrees of freedom on  $\partial P$ , and this creates a sub-triangulation of  $P$ . Taking a clock-wise orientation of  $\partial P$ , we denote the degrees of freedom on  $\partial P$  as  $\{\sigma_l\}_{l=1, \dots, N_P+1}$  with  $\sigma_1 = \sigma_{N_P+1}$  and the sub-triangles will be  $T_l = \{\mathbf{x}^*, \sigma_l, \sigma_{l+1}\}$  for  $l = 1, \dots, N_P$ . The list of sub-triangles in  $P$  is denoted by  $\mathcal{T}_P$ . We identify the average value  $\bar{\mathbf{u}}$  with an approximation of  $\mathbf{u}$  at  $\mathbf{x}^*$ . This has no impact on the accuracy since we are looking for a first order scheme.



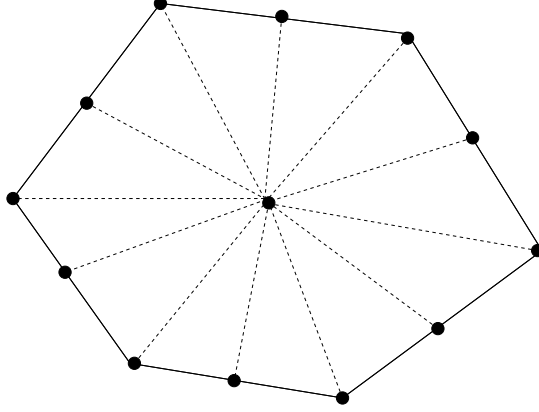


Figure 2: Sub-triangulation that is used to define a low order scheme.

We update the point values by

$$\frac{d\mathbf{u}_\sigma}{dt} + \frac{1}{|C_\sigma|} \sum_{P, \sigma \in P} \Phi_\sigma^P = 0. \quad (25)$$

where  $C_\sigma$  is the dual cell of area

$$|C_\sigma| = \sum_{P, \sigma \in P} \sum_{T \in \mathcal{T}_P, \sigma \in T} \frac{|T|}{3}, \quad (26)$$

and, again inspired by what has been done in the framework of Residual distribution schemes, the so-called residuals are given by

$$\Phi_\sigma^P = \sum_{T \in \mathcal{T}_P, \sigma \in T} \Psi_\sigma^T, \quad (27)$$

with

$$\Psi_\sigma^T = \frac{1}{3} \oint_T \mathbf{A} \cdot \nabla \mathbf{u} \, d\mathbf{x} + \alpha_T (\mathbf{u}_\sigma - \bar{\mathbf{u}}_T), \quad \oint_T \mathbf{A} \cdot \nabla \mathbf{u} \, d\mathbf{x} = \frac{1}{3} \sum_{v \text{ vertex of } T} (\mathbf{A} \cdot \nabla \mathbf{u})_v. \quad (28)$$

Here,  $\alpha_T$  is an upper bound of the spectral radius of  $\mathbf{A}$  evaluated from the two point values of  $T$  and the average value  $\bar{\mathbf{u}}_T$  multiplied by an upper bound of the scaled normals to  $T$ . The scheme is stable under a CFL like condition based on the values of  $\alpha$  and  $|C_\sigma|$ .

**Remark 3.1.** *Another solution could have been to use the Roe scheme. This has been implemented and the results are similar, except for the fact that the Roe scheme is not entropy stable. This has an effect on some test cases, such as the KT test case, see Section 4.2.5.*

### 3.3 Boundary conditions

This section only deals with the Euler equations: all the scalar problems are chosen such that the solution does not change in a neighborhood of the boundary. We need to consider 3 types of boundary conditions: i) wall, ii) inflow/outflow, iii) and Neumann type. We describe what is done first for the average update and then the point values.

#### 3.3.1 Average Values

The problem is to evaluate the flux contribution on the faces  $e$  of a polygon  $P$  which is on the boundary of the computational domain.

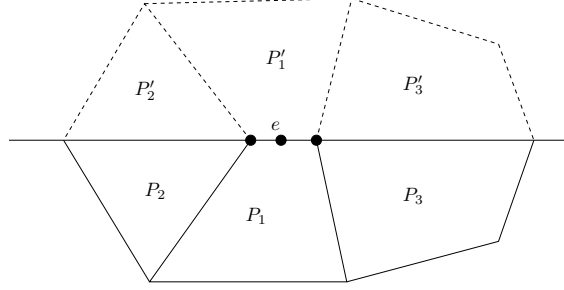


Figure 3: Treatment of Neumann type boundary conditions for the update of average values.

- Wall. The flux at the wall is obtained from a numerical flux  $\hat{\mathbf{f}}_{\mathbf{n}}$  given by

$$\oint_e \hat{\mathbf{f}}_{\mathbf{n}}(\mathbf{u}_e, \mathbf{u}_e^s) d\gamma, \quad (29)$$

where  $\oint$  is a quadrature formula<sup>2</sup>,  $\mathbf{n}$  is the outward unit normal to  $e$ ,  $\mathbf{u}_e = (\rho, \rho\mathbf{v}, E)^T$  represents the polynomial approximation on  $e$ , and  $\mathbf{u}_e^s$  is the state with the same density, the same total energy and the velocity which has been symmetrized with respect to  $\mathbf{n}$ . In practice,  $\hat{\mathbf{f}}_{\mathbf{n}}$  is the Rusanov flux.

If one seek for a first order approximation only, then  $\mathbf{u}_e$  is replaced by the average value of the polygon  $P$ , and  $\mathbf{u}_e^s$  is defined accordingly.

- Inflow/outflow. The flux across the boundary edge  $e$  is evaluated as

$$\oint_e \hat{\mathbf{f}}_{\mathbf{n}}(\mathbf{u}_e, \mathbf{u}^\infty) d\gamma, \quad (30)$$

where  $\mathbf{u}^\infty$  is the state at infinity. To make sure one get complete upwinding for supersonic inflow or outflow, the numerical flux is evaluated as:

$$\hat{\mathbf{f}}_{\mathbf{n}}(\mathbf{u}_e, \mathbf{u}^\infty) = \mathbf{A}_{\mathbf{n}}^+(\mathbf{u}^\infty)\mathbf{u}_e + \mathbf{A}_{\mathbf{n}}^-(\mathbf{u}^\infty)\mathbf{u}^\infty$$

- Neumann type. We refer to Figure 3. For the edge  $e$  of  $P_1$ , we consider the element  $P'_1$  obtained by symetrizing  $P_1$  with respect to the outward normal to  $e$  and we put in  $P'_1$  the same state as in  $P_1$ , then the flux is computed. It is simply

$$\oint_e \mathbf{f}(\mathbf{u}) \cdot \mathbf{n} d\gamma. \quad (31)$$

### 3.3.2 Point values

For the point values, it is again a bit more complicated. The update of the point values localized at the • points depicted in Figure 3 is obtained as

$$\frac{d\mathbf{u}_\sigma}{dt} + \sum_{P, \sigma \in P} \Phi_\sigma^P(\mathbf{u}) = 0,$$

where in the sum we consider the polygons of the triangulation that share  $\sigma$  and we have also included those obtained by symmetrization: the polygons  $P'_1$ ,  $P'_2$  and  $P'_3$  of Figure 3. Here we focus on how we evaluate  $\Phi_\sigma^P$  for  $P$  symmetrized.

<sup>2</sup>We always use the Gauss-Lobatto points since they are our degrees of freedom on the edges.

- Wall. In the symmetrized polygons with state  $(\rho, \rho \mathbf{v}, E)^T$ , we consider the symmetrized state given by  $(\rho, \rho s_{\mathbf{n}}(\mathbf{v}), E)$ . All the geometrical elements are also mirrored with respect to  $e$ .
- Inflow/outflow. We populate the symmetrized elements  $P'$  with the state  $(\rho_{\infty}, \rho_{\infty} \mathbf{v}, E_{\infty})^T$ . The geometrical elements are those of  $P$ .
- Neumann. We feed the symmetrized elements  $P'$  with the state of  $P$ .

For the implementation, we have to take into account that, for the first order scheme, the area  $C_{\sigma}$  is again evaluated as in (26).

### 3.4 Nonlinear stabilization

When the solution develops discontinuities, the high order scheme will be prone to numerical oscillations. To overcome this issue, we have used a simplified version of the MOOD paradigm, see [4, 24]. Since point values and averages are independent variables, we need to test both against a set of admissibility criteria.

The idea is to work with several schemes ranging from order  $k = 3$  to  $k = 1$ , with the lowest order one able to provide results staying in the invariance domain  $\mathcal{D}$ . For the element  $P$ , we write the scheme for  $\bar{\mathbf{u}}_P$  as  $S_P(k)$  and for  $u_{\sigma}$  as  $S_{\sigma}(k)$ , namely for average and point values, respectively.

We denote by  $\mathbf{u}_P^n$  and  $\mathbf{u}_{\sigma}^n$  the solution at the time  $t^n$ . After each Runge-Kutta cycle, the updated solution is denoted by  $\tilde{\mathbf{u}}_P, \tilde{\mathbf{u}}_{\sigma}$ . This is still linear in the sense of Godunov [25], thus it must undergo a limiting procedure.

We first run the high order scheme, for each Runge-Kutta cycle. Concerning the average  $\mathbf{u}_P$ , we store the flux  $\oint_e \mathbf{f}(\mathbf{u}) \cdot \mathbf{n} d\gamma$  for reasons of conservation. Then, for the average solution, we proceed as follows:

1. Computer Admissible Detector (CAD): we check if  $\tilde{\mathbf{u}}_P$  is a valid vector with real components, namely we verify that each component is not NaN. If this is not the case, we flag the element and go to the next one in the list,
2. Physically Admissible Detector (PAD): we check if  $\tilde{\mathbf{u}}_P \in \mathcal{D}$ . If this is false, the element is flagged, and we proceed the control on the next one in the list.
3. Then we check if at  $t^n$ , the solution is not constant in the elements used in the numerical stencil (so we check and compare between the average and point values  $\mathbf{u}_{\sigma}$  in  $P$  with those in the elements sharing a face with  $P$ ). This is done in order to avoid to detect a wrong maximum principle. If the solution is declared locally constant, we move to the next element and we let the polygon  $P$  unflagged.
4. Discrete Maximum Principle (DMP): we check if  $\tilde{\mathbf{u}}_P$  is a local extrema. If we are dealing with the Euler equations, we compute the density and the pressure and perform this test on these two quantities only, even though for a system this is not really meaningful. We denote by  $\xi$  the variable on which we perform the test (i.e.  $\mathbf{u}_P$  itself for scalar problems, and the density/pressure for the Euler system). Let  $\mathcal{V}(P)$  be the set of elements  $F$  that share a face or a vertex with  $P$ , excluding  $P$  itself. We say that we have a potential extrema if

$$\tilde{\xi}_P^{n+1} \notin [(\min_{F \in \mathcal{V}(P)} \xi_F^n) - \varepsilon_P^n, (\max_{F \in \mathcal{V}(P)} \xi_F^n) + \varepsilon_P^n],$$

where  $\varepsilon_P^n$  is a parameter estimated as in [4]. If the above test is true, the element is flagged.

If an element is flagged, then each of its faces are flagged, and we recompute the flux of the flagged faces using the first order scheme.

For the point values, the procedure is similar, and then for the flagged degrees of freedom, we recompute the residuals

$$\sum_{P, \sigma \in P} \Phi_{\sigma}^P(\mathbf{u}^n)$$

with the first order scheme.

## 4 Results

In this section, we demonstrate the robustness and effectiveness of the proposed scheme on a number of classical numerical examples, some are challenging.

### 4.1 Scalar case

#### 4.1.1 Convection case

$$\frac{\partial u}{\partial t} + \mathbf{a} \cdot \nabla u = 0, \quad u_0(x) = \exp(-20\|\mathbf{x} - \mathbf{x}_0\|^2). \quad (32)$$

We run this case on the domain  $[-20, 20]^2$ , the velocity field is  $\mathbf{a} = 2\pi(-y, x)$  and  $\mathbf{x}_0 = (1, 1)$  for one full rotation, i.e.  $t_f = 1$ . The errors for a triangular mesh are given in Table 1. A similar set of simulations is conducted using the same family of meshes but for which we generate the dual cells, which yield our family of polygonal meshes. The errors as well as the convergence order of the new schemes are given in Table 2, confirming that the formal third order of accuracy is achieved in all cases: the meshes are not generated by subdividing "caorse" meshes into finer meshes, but we only control the mesh resolution from the point value distribution on the boundary of the computational domain. In that case, the best we can hope, as for any finite element type method, is a one order  $k + 1/2$ , i.e. 2.5 here.

Average values						
$h$	$L^\infty$	slope	$L^1$	slope	$L^2$	slope
0.148	0.410	-	$3.08 \cdot 10^{-2}$	-	$7.30 \cdot 10^{-3}$	-
$7.43 \cdot 10^{-2}$	0.166	1.30	$1.128 \cdot 10^{-2}$	1.72	$2.22 \cdot 10^{-3}$	1.71
$3.88 \cdot 10^{-2}$	$3.57 \cdot 10^{-2}$	2.36	$2.255 \cdot 10^{-3}$	2.65	$3.98 \cdot 10^{-4}$	2.65
$1.85 \cdot 10^{-2}$	$4.94 \cdot 10^{-3}$	2.68	$3.02 \cdot 10^{-4}$	2.72	$5.33 \cdot 10^{-5}$	2.72
$4.64 \cdot 10^{-3}$	$1.16 \cdot 10^{-4}$	2.70	$6.53 \cdot 10^{-6}$	2.64	$1.37 \cdot 10^{-6}$	2.64
Point values						
$h$	$L^\infty$	slope	$L^1$	slope	$L^2$	slope
0.148	0.426	-	$5.21 \cdot 10^{-3}$	-	$2.72 \cdot 10^{-2}$	-
$7.43 \cdot 10^{-2}$	0.175	1.28	$1.54 \cdot 10^{-3}$	1.75	$9.48 \cdot 10^{-3}$	1.52
$3.88 \cdot 10^{-2}$	$3.83 \cdot 10^{-2}$	2.34	$2.68 \cdot 10^{-4}$	2.69	$1.85 \cdot 10^{-3}$	2.51
$1.85 \cdot 10^{-2}$	$5.44 \cdot 10^{-3}$	2.65	$3.69 \cdot 10^{-5}$	2.68	$2.45 \cdot 10^{-4}$	2.75
$4.64 \cdot 10^{-3}$	$1.42 \cdot 10^{-4}$	2.63	$1.63 \cdot 10^{-6}$	2.25	$8.21 \cdot 10^{-6}$	2.45

Table 1: Errors for the average and point values, triangular mesh, rotation problem (32), scheme (15)–(20)–(21)–(23), 1 rotation.

#### 4.1.2 KPP case

This problem has been considered by Kurganov, Popov and Petrova in [26]. It writes

$$\frac{\partial u}{\partial t} + \frac{\partial(\sin u)}{\partial x} + \frac{\partial(\cos u)}{\partial y} = 0, \quad (33)$$

in a domain  $[-2, 2]^2$  with the initial condition

$$u_0(\mathbf{x}) = \begin{cases} \frac{7}{2}\pi & \text{if } \|\mathbf{x} - (0, 0.5)\|^2 \leq 1, \\ \frac{\pi}{4} & \text{else.} \end{cases}$$

The problem (33) is non-convex, in the sense that compound waves may exist. Here, we have used the MOOD paradigm with the Local Lax-Friedrichs scheme as a first order scheme. We compute the numerical solution

Average values						
$h$	$L^\infty$	slope	$L^1$	slope	$L^2$	slope
0.224	0.354	-	$1.107 \cdot 10^{-2}$	-	$3.91 \cdot 10^{-2}$	-
0.112	0.241	0.560	$4.475 \cdot 10^{-3}$	1.310	$1.877 \cdot 10^{-2}$	1.060
$5.602 \cdot 10^{-2}$	$7.36 \cdot 10^{-2}$	2.58	$9.580 \cdot 10^{-4}$	2.224	$4.694 \cdot 10^{-3}$	2.000
$2.801 \cdot 10^{-2}$	$1.230 \cdot 10^{-2}$	2.58	$1.577 \cdot 10^{-4}$	2.603	$7.300 \cdot 10^{-4}$	2.685
$h$	$L^\infty$	slope	$L^1$	slope	$L^2$	slope
Point values						
0.224	0.575	-	$8.389 \cdot 10^{-3}$	-	$3.622 \cdot 10^{-2}$	-
0.112	0.281	0.559	$3.146 \cdot 10^{-3}$	1.415	$1.606 \cdot 10^{-2}$	1.173
$5.602 \cdot 10^{-2}$	$7.695 \cdot 10^{-2}$	1.709	$6.927 \cdot 10^{-4}$	2.183	$3.922 \cdot 10^{-3}$	2.033
$2.801 \cdot 10^{-2}$	$1.277 \cdot 10^{-2}$	2.582	$1.233 \cdot 10^{-4}$	2.490	$6.233 \cdot 10^{-4}$	2.654

Table 2: Errors for the average and point values, polygonal mesh mesh, rotation problem (32), scheme (15)–(20)–(21)–(23), 1 rotation.

until the final time  $t_f = 1$ . The triangular mesh has 29909 point value DoFs, 14794 triangular polygons and 22351 faces. The mesh is represented in Figure 4-(a). The polygonal mesh has 38425 point value DoFs, 7558 elements and 22991 faces. Though the number of point value DoFs is larger for the polygonal mesh, the resolution of the polygonal mesh is similar to that of the triangular one. The reason is that, as this can be seen in Figure 4-(d), the polygons have in general 6 edges, so we have 12 DoFs, while the triangles have only 6 DoFs. The ratio is about 2. Looking at Figure 4-(c), the results are similar.

The results we obtain are in agreement with published results. In particular, we have managed to have a good shock structure. In that respect, the use of Rusanov scheme for the point values and local Lax Friedrichs flux for the average values, combined with the MOOD technique is important: if we were using the Roe scheme for the average values and/or its variants for the point values, we would not get a correct shock structure. This is an experimental fact.

## 4.2 System case

### 4.2.1 Acoustics

For  $\mathbf{u} \in \mathbb{R}^2$  and  $p \in \mathbb{R}$ , the acoustics system reads

$$\begin{cases} \frac{\partial \mathbf{u}}{\partial t} + \nabla p = 0 \\ \frac{\partial p}{\partial t} + c^2 \operatorname{div} \mathbf{u} = 0 \end{cases}. \quad (34)$$

In [27], it was mentioned that Active flux on Cartesian meshes manages to preserve very well the steady solutions of (34). For that, besides a theoretical analysis, examples of the following problem is shown:

$$p(\mathbf{x}, t = 0) = 0, \quad \mathbf{u} = \begin{cases} 0 & \text{if } \|\mathbf{x}\| \geq 0.4, \\ (2 - 5\|\mathbf{x}\|) \frac{\mathbf{x}}{\|\mathbf{x}^\perp\|} & \text{if } 0.2 \leq \|\mathbf{x}\| \leq 0.4, \\ 5\mathbf{x}^\perp & \text{if } 0 \leq \|\mathbf{x}\| \leq 0.2, \end{cases} \quad (35)$$

where for  $\mathbf{x} = (a, b)$ ,  $\mathbf{x}^\perp = (-b, a)$ . In (34), we set  $c = 1$ , and run the scheme until  $t_f = 100$  in the domain  $[-1, 1]^2$ . The problem (35) is a steady problem, so the solution should not change. Note that the mesh has no particular symmetry and it is not particularly regular (it has been obtained with the option Delaunay in meshing with GMSH). Figure 5 shows the norm of the velocity field at time  $t_f = 100$ , as well as the meshes that have been used. The scatter plots depicted in Figure 6 confirm that the solution has very little dispersion and is almost equal to the initial condition. Notice that the meshes are very coarse. This seems

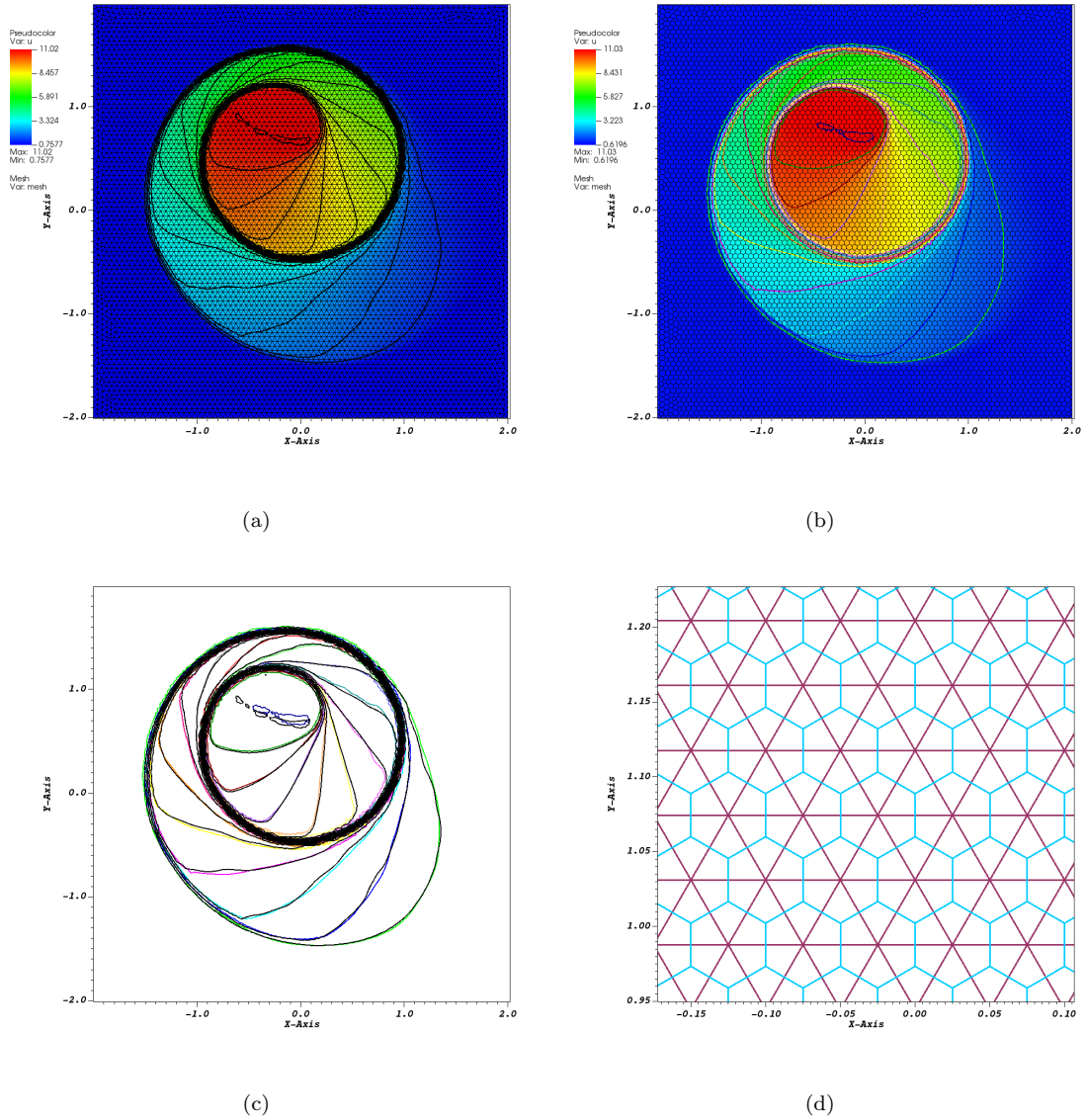


Figure 4: KPP problem using quadratic approximation. (a) The mesh is triangular. (b) The mesh is polygonal. (c) Comparison with the two solutions. Colored : solution with triangle. Black: solution with polygons. (d) Computational meshes. The CFL is 0.3.

to indicate that this kind of schemes also have a very good behavior with respect to irrotational flows, as explained in [27]. However, the explanation is likely to be different because the schemes, and the meshes are very different.

#### 4.2.2 Euler equations

Four cases are considered: the moving vortex case, two examples of 2D Riemann problems, and the double Mach reflection case.

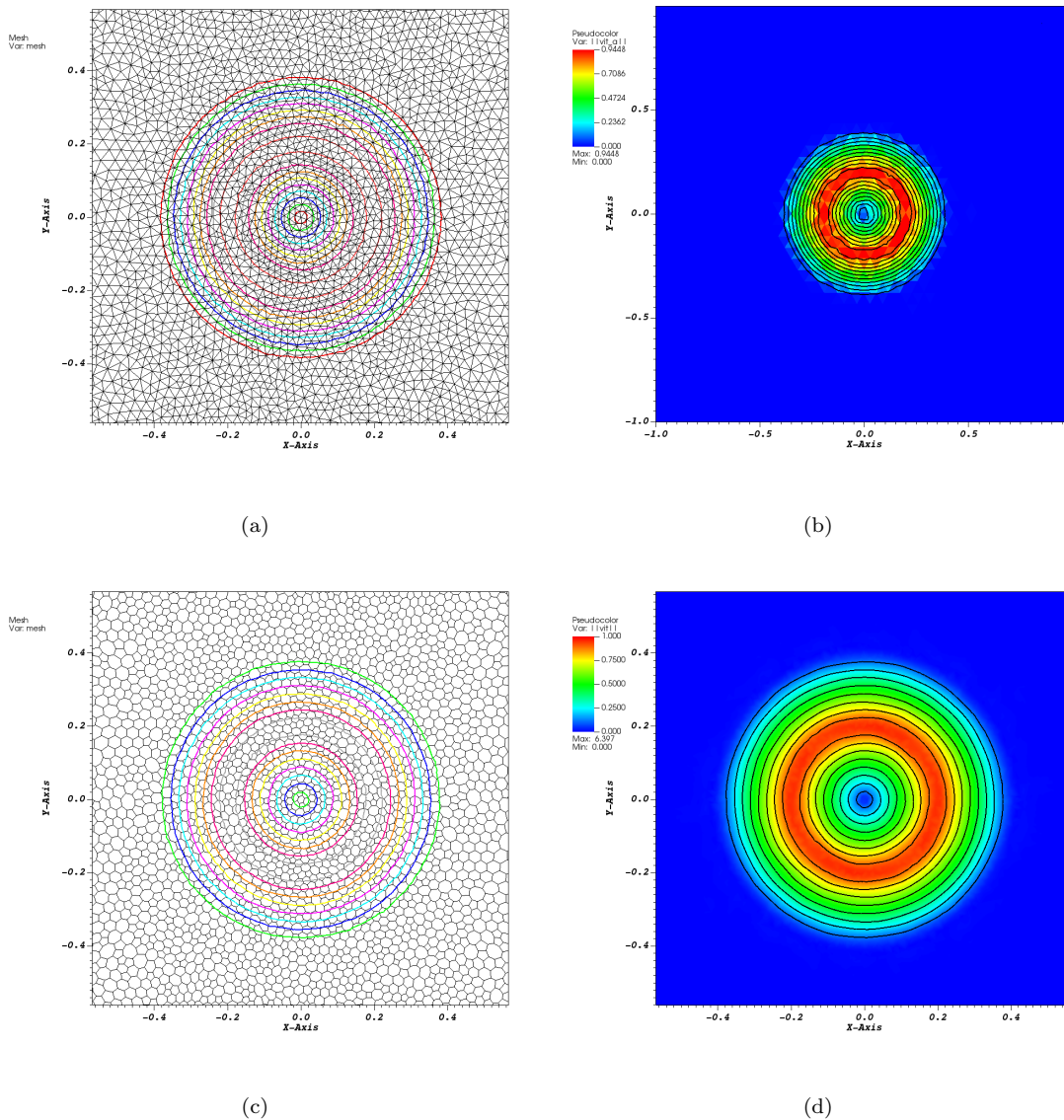


Figure 5: Acoustics: plots of the velocity and the computational mesh. Left: average values. Right: point values.

### 4.2.3 Moving vortex case

In the first example of nonlinear Euler equations, a moving vortex case is defined in the computational domain  $[-20, 20]^2$ . The final time of the simulation is  $t_f = 20$ , and the initial condition is given by

$$\begin{aligned}
 u &= u_\infty - \mathbf{y}_2 e^{\frac{1-R}{2}}, v = v_\infty + \mathbf{y}_1 e^{\frac{1-R}{2}}, \\
 \rho &= (T_\infty + \Delta T)^{1/(\gamma-1)}, \Delta T = -\frac{\gamma-1}{2\gamma} M^2 e^{1-R}, \\
 p &= \rho^\gamma,
 \end{aligned}$$

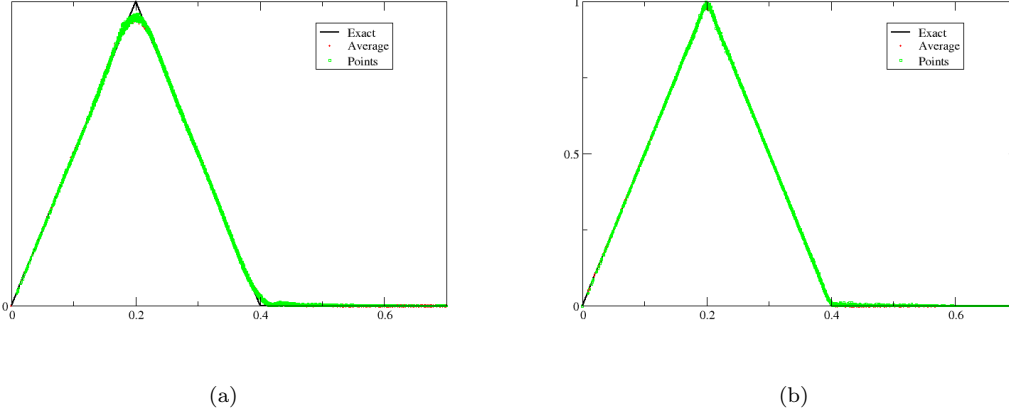


Figure 6: Acoustics: scatter plots of the velocity norm, compared to the exact solution. (a): polygonal mesh. (b): triangular mesh.

with

$$\mathbf{u}_\infty = (1, \sqrt{2}/2), \quad \mathbf{y} = \mathbf{x}/2, \quad T_\infty = 1, \quad r_0 = 1, \quad \beta = 5, \quad M = \frac{\beta}{4\pi}, \quad R = \frac{\|\mathbf{y}\|^2}{r_0^2}.$$

The solution computed on a polygonal mesh with 18252 point DoFs and 3565 elements is shown in Figure 7-(a). Additionally, a comparison with the exact solution is depicted in Figure 7-(b), where the exact solution is obtained by advecting the vortex with the velocity  $(u_\infty, v_\infty)$ .

#### 4.2.4 Liu-Lax problem

In the second example of nonlinear Euler equations ~~system-cases~~, we consider the following initial condition

$$(\rho, u, v, p) = \begin{cases} (\rho_1, u_1, v_1, p_1) = (0.5313, 0, 0, 0.4) & \text{if } x \geq 0 \text{ and } y \geq 0, \\ (\rho_2, u_2, v_2, p_2) = (1, 0.7276, 0, 1) & \text{if } x \leq 0 \text{ and } y \geq 0, \\ (\rho_3, u_3, v_3, p_3) = (0.8, 0, 0, 1) & \text{if } x \leq 0 \text{ and } y \leq 0, \\ (\rho_4, u_4, v_4, p_4) = (1, 0, 0.7276, 1) & \text{if } x \geq 0 \text{ and } y \leq 0, \end{cases}$$

prescribed in the computational domain  $[-2, 2]^2$ . The states 1 and 2 are separated by a shock. The states 2 and 3 are separated by a slip line. The states 3 and 4 are separated by a steady slip-line. The states 4 and 1 are separated by a shock. The mesh corresponds to a  $400 \times 400$  cells, i.e. with 481601 DoFs. The obtained results of the density field are plotted in Figure 8. The results are qualitatively coherent with those obtained in the literature.

#### 4.2.5 Kurganov-Tadmor problem

In the third example of nonlinear Euler equations ~~system-cases~~, the initial condition is

$$(\rho, u, v, p) = \begin{cases} (\rho_1, u_1, v_1, p_1) = (1.5, 0, 0, 1.5) & \text{if } x \geq 1 \text{ and } y \geq 1, \\ (\rho_2, u_2, v_2, p_2) = (0.5323, 1.206, 0, 0.3) & \text{if } x \leq 1 \text{ and } y \geq 1, \\ (\rho_3, u_3, v_3, p_3) = (0.138, 1.206, 1.206, 0.029) & \text{if } x \leq 1 \text{ and } y \leq 1, \\ (\rho_4, u_4, v_4, p_4) = (0.5323, 0, 1.206, 0.3) & \text{if } x \leq 1 \text{ and } y \leq 1. \end{cases}$$

Here, the four states are separated by shocks. The domain is  $[-2, 2]^2$ . The solution at  $t_f = 3$  is displayed in Figure 9. The mesh has again  $400 \times 400$  cells, i.e. with 481601 DoFs. We see that, on the one hand,



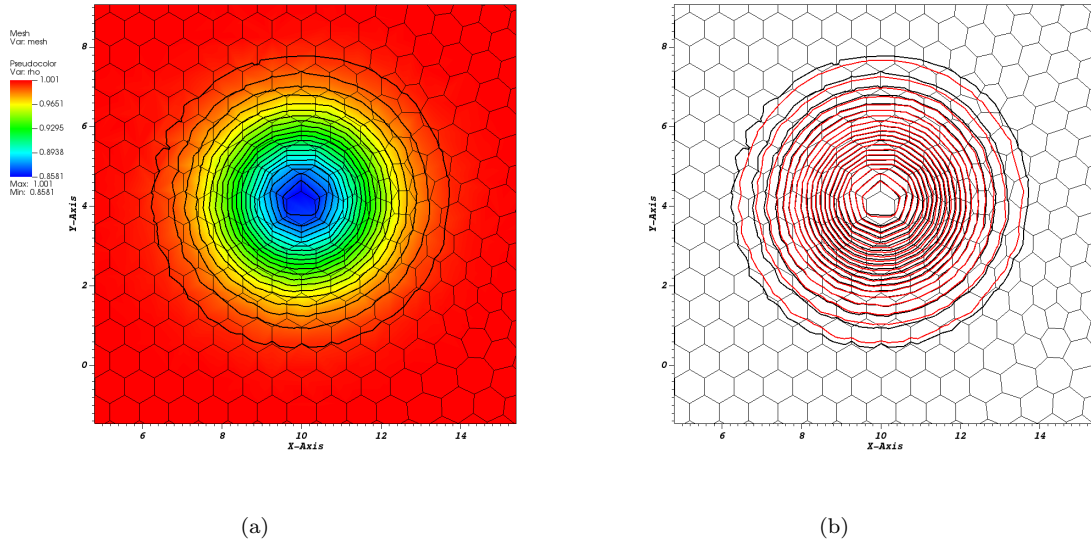


Figure 7: Moving vortex. (a): Plot of the density for the vortex problem, with 20 equally spaced isolines. (b): Comparison between the exact solution (red) and the numerical one. The final time is  $t_f = 20$ . The domain is  $[-20, 20]^2$ , the scheme is (18)-(20)-(21). The CFL is 0.2. The mesh has 18252 point DoFs and 3565 cells.

the solution looks very similar to what was obtained in the literature, see e.g. [3, 28, 29, 30]. On the other hand, the first-order schemes (for average and point values) are activated on very few positions, see Figures 9-c and 9-d.

The results are in agreement with what is obtained in the literature. The density isolines plot indicates noise in the right upper quadrant. The pressure isoline plot does not show this. This is probably due to some problems in the nonlinear stabilisation. Indeed, the two plots that represent where the first order scheme is needed show that the flag behaves differently: some work needs to be done, or a completely different stabilisation mechanism might be constructed. This is the subject of a future work.

#### 4.2.6 DMR case

The final test case is the double Mach reflection problem. The domain consists of a ramp of 30 degrees. The initial condition corresponds to a Mach 10 shock in a quiescent flow, where the pressure is chosen to be  $p = 1$  and the density is  $\rho = \gamma$  with  $\gamma = 1.4$ . The mesh has 1,555,600 point DoFs and 776,501 triangular polygons. This corresponds to a resolution of  $h = 1/N$  with  $N \approx 350$ . For  $t_f = 0.18$ , a zoom of the density is represented in Figure 10, as well as the computational mesh. This allows to get an idea of the width of the contact line and the shocks. We notice the appearance of a roll-up structure on the slip line. In this simulation, the MOOD detector on the points is almost never activated quite early after the initialisation. The detector on the average is activated more often. This translates in practice by some wiggles on the density (not represented), but the simulation remains stable.

## 5 Conclusion and perspectives

We have presented a way to generalize the method of [3] to arbitrary polygonal control volumes using an approximation method inspired by the VEM technology. Here, we only use the VEM to replace the polynomial approximation of [3] by a polynomial-free approximation. More precisely, we can discretize the

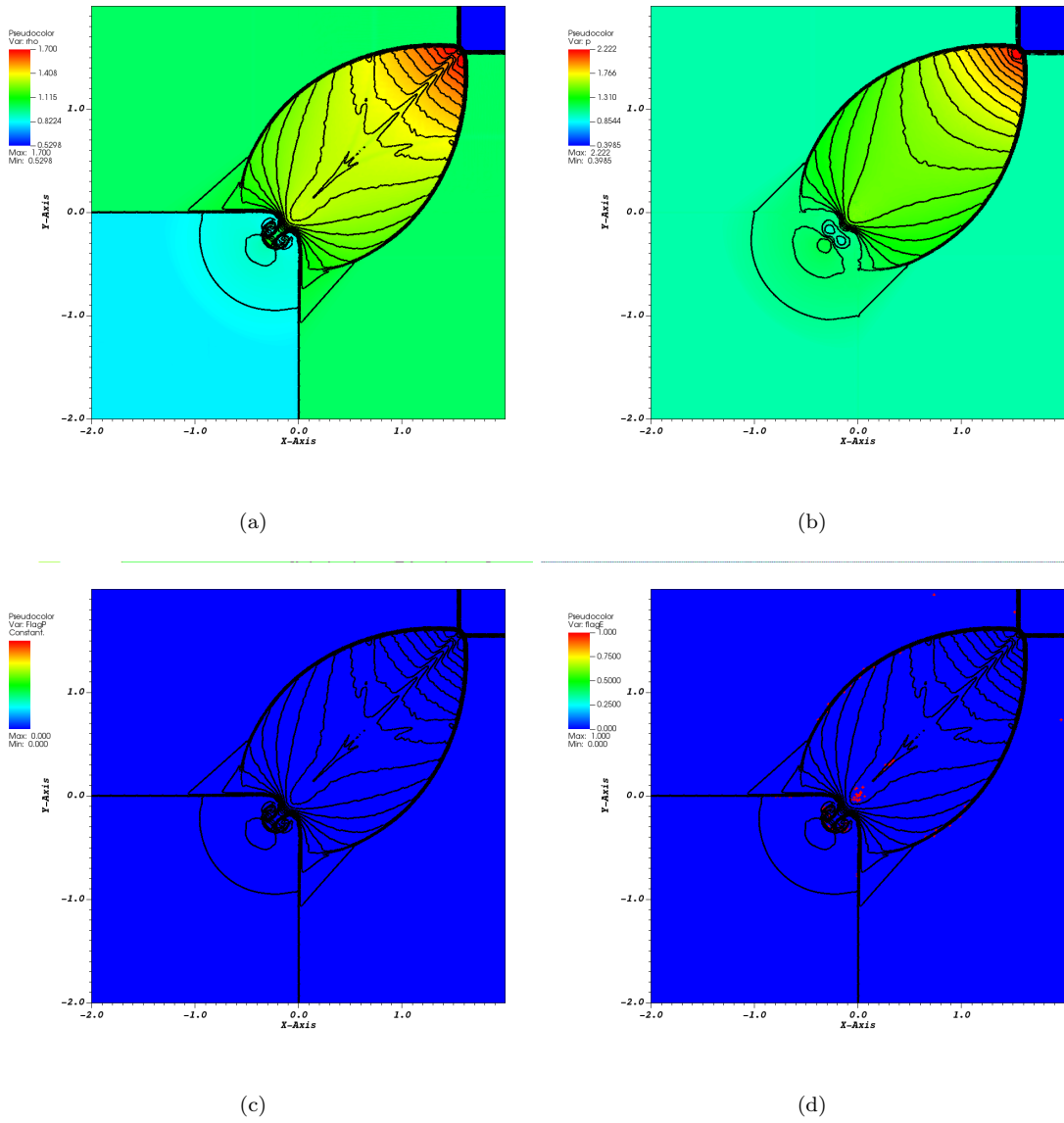


Figure 8: Lax-Liu test case. (a) Density. (b) Pressure. (c) In red where the first order scheme is applied for the point scheme. (d) In red where the first order scheme is applied for the average scheme. 30 isolines  $\rho \in [0.5298, 1.700]$ ,  $p \in [0.3985, 2.222]$ . CFL=0.3. The mesh is  $400 \times 400$ .

gradients using only the degrees of freedom, and not by using explicitly constructed basis functions. We have shown on several examples that the method preserves its stability and its accuracy, and may have surprisingly good results for the acoustic problem.

However, this is not the end of the story. In order to be able to compute solutions with shocks, we need to introduce, as usual, some nonlinear mechanism. This is done here, as in the above mentioned paper, by using the MOOD paradigm. We have relied on a rather crude implementation of this method (in fact exactly the same as in [3]), but the results appear to be slightly less satisfactory. For this reason, we are currently working on a bound preserving technique that can adapt to the current setting. We also intend to extend

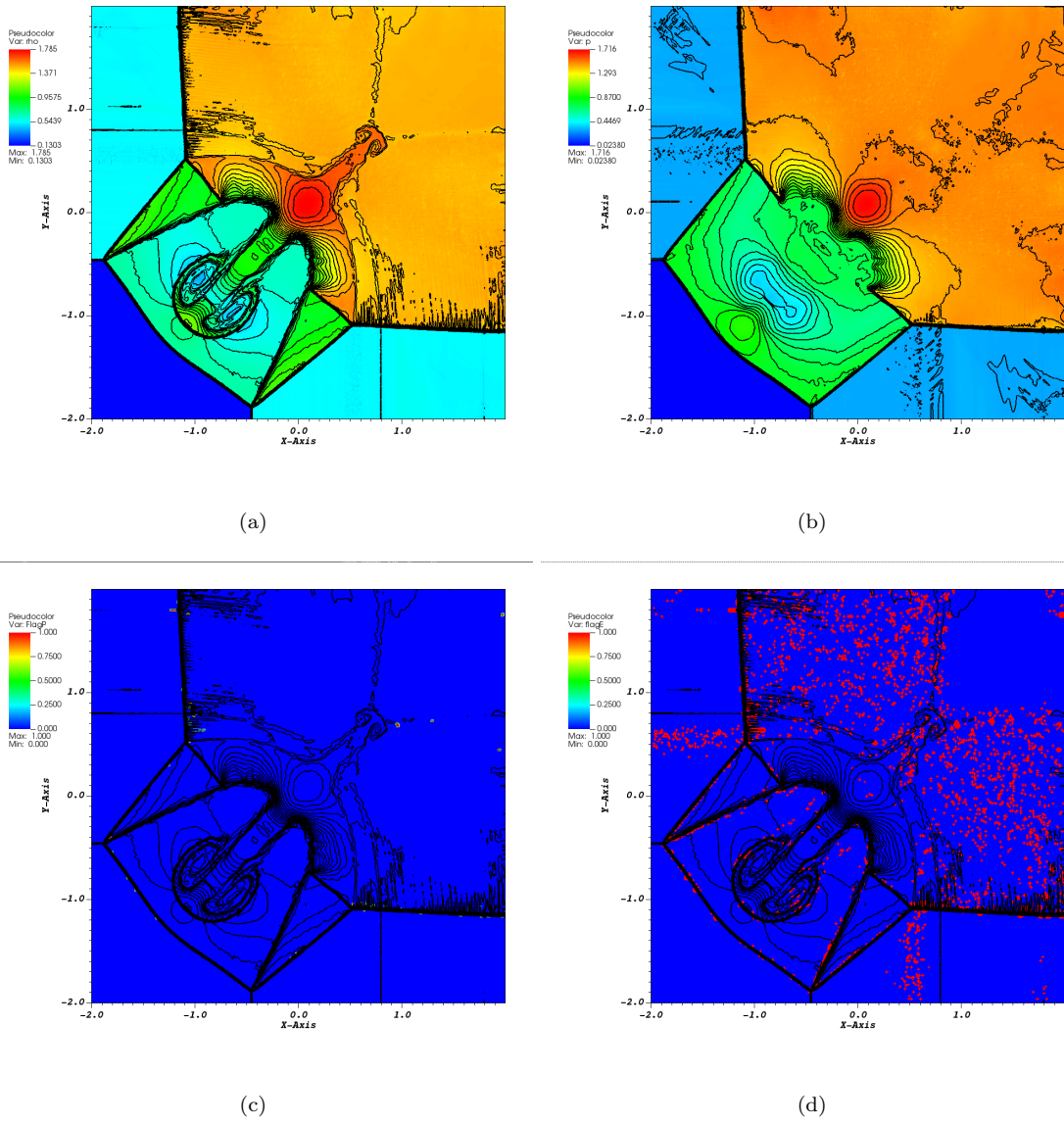


Figure 9: Kurganov-Tadmor test case. (a) Density. (b) Pressure. (c) In red where the first order scheme is applied for the point scheme. (d) In red where the first order scheme is applied for the average scheme. 30 isolines  $\rho \in [0.130, 1.785]$ ,  $p \in [0.0238, 1.716]$ . CFL=0.3. The mesh is  $400 \times 400$ .

the method to higher than formally third order of accuracy following [9].

## Acknowledgements

The work of YL was supported by UZH Postdoc Grant, 2024 / Verfügung Nr. FK-24-110 and SNFS grant 200020\_204917 "Solving advection dominated problems with high order schemes with polygonal meshes: application to compressible and incompressible flow problems". WB acknowledges research funding by

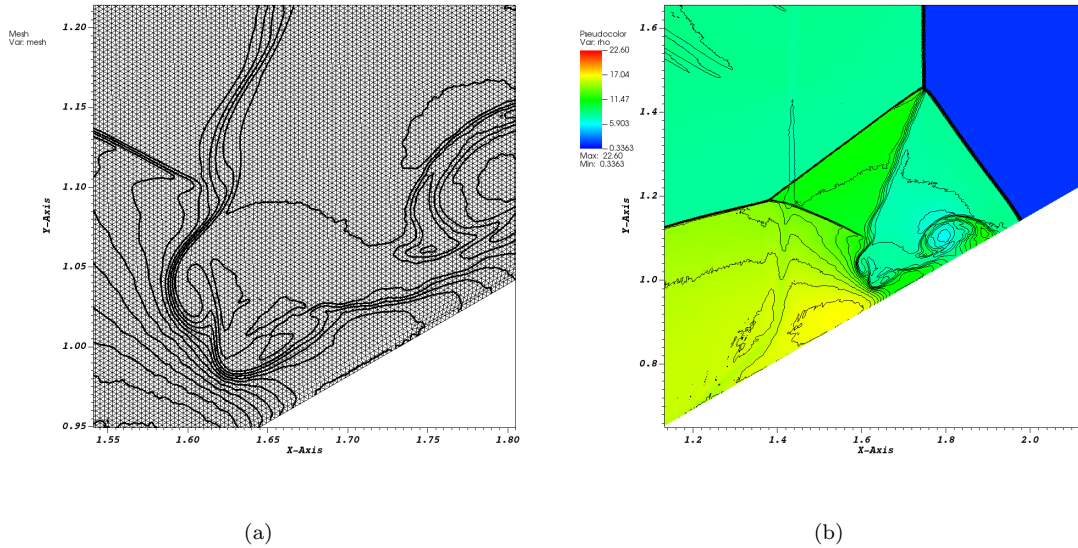


Figure 10: DMR test case. (a) Density isolines and computational mesh. (b) Density (average) isolines with color plot of the average (points). 30 isolines. CFL=0.3. For the mesh, all the sub-elements are represented.

Fondazione Cariplo and Fondazione CDP (Italy) under the project No. 2022-1895 and by the Italian Ministry of University and Research (MUR) in the framework of the PRIN 2022 project No. 2022N9BM3N.

## References

- [1] T.A. Eyman and P.L. Roe. Active flux. 49th AIAA Aerospace Science Meeting, 2011.
- [2] R. Abgrall. A combination of residual distribution and the active flux formulations or a new class of schemes that can combine several writings of the same hyperbolic problem: application to the 1d Euler equations. *Commun. Appl. Math. Comput.*, 5(1):370–402, 2023.
- [3] Rémi Abgrall, Jianfang Lin, and Yongle Liu. Active flux for triangular meshes for compressible flows problems. *Beijing Journal of Pure and Applied Mathematics*, in press. also Arxiv preprint 2312.11271.
- [4] S. Clain, S. Diot, and R. Loubère. A high-order finite volume method for systems of conservation laws—Multi-dimensional Optimal Order Detection (MOOD). *J. Comput. Phys.*, 230(10):4028–4050, 2011.
- [5] T.A. Eyman and P.L. Roe. Active flux for systems. 20 th AIAA Computational Fluid Dynamics Conference, 2011.
- [6] T.A. Eyman. *Active flux*. PhD thesis, University of Michigan, 2013.
- [7] C. Helzel, D. Kerkmann, and L. Scandurra. A new ADER method inspired by the active flux method. *Journal of Scientific Computing*, 80(3):35–61, 2019.
- [8] W. Barsukow. The active flux scheme for nonlinear problems. *J. Sci. Comput.*, 86(1):Paper No. 3, 34, 2021.

- [9] Remi Abgrall and Wasilij Barsukow. Extensions of active flux to arbitrary order of accuracy. ESAIM, Math. Model. Numer. Anal., 57(2):991–1027, 2023.
- [10] Junming Duan, Wasilij Barsukow, and Christian Klingenberg. Active flux methods for hyperbolic conservation laws – flux vector splitting and bound-preservation: One-dimensional case, 2024.
- [11] Junming Duan, Wasilij Barsukow, and Christian Klingenberg. Active flux methods for hyperbolic conservation laws – flux vector splitting and bound-preservation: Two-dimensional case, 2024.
- [12] M. Shashkov. Conservative finite-difference methods on general grids. Ed. by Stanly Steinberg. Incl. 1 disk. Boca Raton, FL: CRC Press, 1996.
- [13] L. Beirão da Veiga, Franco Brezzi, L. D. Marini, and A. Russo. The Hitchhiker’s guide to the virtual element method. Math. Models Methods Appl. Sci., 24(8):1541–1573, 2014.
- [14] Lourenço Beirão da Veiga, Franco Brezzi, L. Donatella Marini, and Alessandro Russo. The virtual element method. Acta Numerica, 32:123–202, 2023.
- [15] Daniele A. Di Pietro, Jérôme Droniou, and Francesca Rapetti. Fully discrete polynomial de Rham sequences of arbitrary degree on polygons and polyhedra. Math. Models Methods Appl. Sci., 30(9):1809–1855, 2020.
- [16] C. Geuzaine and J.-F. Remacle. Gmsh: a three-dimensional finite element mesh generator with built-in pre- and post-processing facilities. International Journal for Numerical Methods in Engineering, 79(11):1309–1331, 209.
- [17] Pierre-Henri Maire. A unified sub-cell force-based discretization for cell-centered lagrangian hydrodynamics on polygonal grids. International Journal for Numerical Methods in Fluids, 65(11-12):1281–1294, 2011.
- [18] Walter Boscheri, Michael Dumbser, and Pierre-Henri Maire. A new thermodynamically compatible finite volume scheme for lagrangian gas dynamics. SIAM Journal on Scientific Computing, 46(4):A2224–A2247, 2024.
- [19] Walter Boscheri and Giacomo Dimarco. High order central weno-implicit-explicit runge kutta schemes for the bgk model on general polygonal meshes. Journal of Computational Physics, 422:109766, 2020.
- [20] Walter Boscheri. A space-time semi-lagrangian advection scheme on staggered voronoi meshes applied to free surface flows. Computers and Fluids, 202:104503, 2020.
- [21] Stefano Berrone and Andrea Borio. Orthogonal polynomials in badly shaped polygonal elements for the virtual element method. Finite Elements in Analysis and Design, 129:14–31, 2017.
- [22] H. Deconinck and M. Ricchiuto. Encyclopedia of Computational Mechanics, chapter Residual distribution schemes: foundation and analysis. John Wiley & sons, 2007. DOI: 10.1002/0470091355.ecm054.
- [23] R. Abgrall. Toward the ultimate conservative scheme: Following the quest. J. Comput. Phys., 167(2):277–315, 2001.
- [24] F. Vilar. *A posteriori* correction of high-order discontinuous Galerkin scheme through subcell finite volume formulation and flux reconstruction. J. Comput. Phys., 387:245–279, 2019.
- [25] S.K.Godunov. A finite difference method for the computation of discontinuous solutions of the equations of fluid dynamics. Mat. Sbornik, 47:357–393, 1959.
- [26] Alexander Kurganov, Guergana Petrova, and Bojan Popov. Adaptive semidiscrete central-upwind schemes for nonconvex hyperbolic conservation laws. SIAM J. Sci. Comput., 29(6):2381–2401, 2007.

- [27] Wasilij Barsukow, Jonathan Hohm, Christian Klingenberg, and Philip L. Roe. The active flux scheme on Cartesian grids and its low Mach number limit. J. Sci. Comput., 81(1):594–622, 2019.
- [28] A. Kurganov, Y. Liu, and V. Zeitlin. Numerical dissipation switch for two-dimensional central-upwind schemes. ESAIM Mathematical Modelling and Numerical Analysis, 55:713–734, 2021.
- [29] N. K. Grag, A. Kurganov, and Y. Liu. Semi-discrete central-upwind Rankine-Hugoniot schemes for hyperbolic systems of conservation laws. Journal of Computational Physics, 428:110078, 2021.
- [30] B.-S. Wang, W. Don, A. Kurganov, and Y. Liu. Fifth-order A-WENO schemes based on the adaptive diffusion central-upwind Rankine-Hugoniot fluxes. Communications on Applied Mathematics and Computation, 5:295–314, 2023.
- [31] B. Ahmed, A. Alsaedi, F. Brezzi, L.D. Marini, and A. Russo. Projectors for Virtual Element Methods. Comput. Math. Appl., 66(3), 2013.

## A VEM approximation: basic facts

Any basis of  $V_k(P)$  is virtual, meaning that it is not explicitly computed in closed form. Consequently, the evaluation of  $v_h(\mathbf{x})$  at some  $\mathbf{x} \in P$  it is not straightforward. One way to proceed would be to evaluate  $\pi(v_h)$ , that is the  $L^2$  projection of  $v_h$  on  $\mathbb{P}_k(P)$ . Since we want to do it only using the degrees of freedom, it turns out that this is impossible in practice. But, as shown in [13, 31], it is possible to define a space  $W_k(P)$  for which computing the  $L^2$  projection is feasible. It is constructed from  $V_k(P)$  in two steps. First, we consider the approximation space  $\tilde{V}_k(P)$  given by

$$\tilde{V}_k(P) = \{v_h, v_h \text{ is continuous on } \partial P \text{ and } (v_h)_{\partial P} \in \mathbb{P}_k(\partial P); \text{ and } \Delta v_h \in \mathbb{P}_k(P)\}.$$

For  $p \in \mathbb{N}$ , let  $M_p^*(P)$  be the vector space generated by the scaled monomial of degree  $p$  exactly,

$$m \in M_p^*(P), \quad m = \sum_{\alpha, |\alpha|=p} \beta_\alpha m_\alpha.$$

Then, we consider  $W_k(P)$ , which is the subspace of  $\tilde{V}_k(P)$  defined by

$$W_k(P) = \{w_h \in \tilde{V}_k(P), \langle w_h - \pi^\nabla w_h, q \rangle = 0, \quad \forall q \in M_{k-2}^*(P) \cup M_k^*(P)\}.$$

In [31], it is shown that  $\dim V_k(P) = \dim W_k(P)$ .

This approximation space is defined as follows.  $w_h \in W_k(P)$  if and only if

1.  $w_h$  is a polynomial of degree  $k$  on each edge  $e$  of  $P$ , that is  $(w_h)|_e \in \mathbb{P}_k(e)$ ,
2.  $w_h$  is continuous on  $\partial P$ ,
3.  $\Delta w_h \in \mathbb{P}_k(P)$ ,
4.  $\int_P w_h m_\alpha \, d\mathbf{x} = \int_P \pi^\nabla w_h m_\alpha \, d\mathbf{x}$  for  $|\alpha| = k - 1, k$ .

The degrees of freedom are the same as in  $V_k(P)$ :

1. The value of  $w_h$  on the vertices of  $P$ ,
2. On each edge of  $P$ , the value of  $v_k$  at the  $k - 1$  internal points of the  $k + 1$  Gauss-Lobatto points on this edge,
3. The moments up to order  $k - 2$  of  $w_h$  in  $P$ ,

$$m_\alpha(w_h) := \frac{1}{|P|} \int w_h m_\alpha \, d\mathbf{x}, \quad |\alpha| \leq k - 2.$$

The  $L^2$  projection of  $w_h$  is computable. For any  $\beta$ , if  $\pi^0(w_h) = \sum_{\alpha, |\alpha| \leq k} s_\alpha m_\alpha$ , we have

$$\langle \pi^0(w_h), m_\beta \rangle = \sum_{\alpha, |\alpha| \leq k} s_\alpha \langle m_\beta, m_\alpha \rangle = \langle w_h, m_\beta \rangle.$$

The left hand side is computable since the inner product  $\langle m_\beta, m_\alpha \rangle$  only involves monomials. We need to look at the right hand side. If  $|\alpha| \leq k - 2$ ,  $\langle w_h, m_\beta \rangle = |P| m_\beta(w_h)$  and if  $|\alpha| = k - 1$  or  $k$ , we have

$$\langle w_h, m_\beta \rangle = \langle \pi^\nabla w_h, m_\alpha \rangle,$$

which is computable from the degrees of freedom only.

We note that if  $w_h \in W_k(P)$ , then  $m_\alpha(\pi^0 w_h) = m_\alpha(w_h)$ . Indeed

$$m_\alpha(\pi^0 w_h) = \frac{1}{|P|} \langle \pi^0 w_h, m_\alpha \rangle = \frac{1}{|P|} \langle w_h, m_\alpha \rangle$$

by construction. This is not true for  $\pi^\nabla$  in  $V_k(P)$ . However, for  $k \leq 2$ ,  $V_k(P) = W_k(P)$

The last remark is that, since  $\mathbb{P}_k(P) \subset V_k(P)$  and  $\mathbb{P}_k(P) \subset W_k(P)$ , the projections of  $C^{k+1}(E)$  onto  $V_k(P)$  and  $W_k(P)$  defined by the degrees of freedom is  $k + 1$ -th order accurate.

## B The N matrix

In this section, we consider  $p \times p$  matrices.

Here, we show that  $\mathbf{N}_\sigma = (\sum_{P, \sigma \in P} K_\sigma^+)^{-1}$  has a meaning when

$$K_\sigma = A_x n_x^P + A_y n_y^P, \quad \forall \mathbf{n}^P = (n_x^P, n_y^P),$$

where  $A_x$  and  $A_y$  are the Jacobian of a symmetrizable system, the vectors  $\mathbf{n}^P$  sum up to 0,

$$\sum_P \mathbf{n}^P = \mathbf{0}$$

and

$$\mathbf{N}_\sigma^{-1} = \sum_P K_\sigma^+.$$

There exists  $A_0$  a symmetric positive definite matrix such that  $A_0 A_x$  and  $A_0 A_y$  are symmetric. For the Euler equations, this is the Hessian of the entropy. From this we see that

$$(A_0 K_\sigma)^+ = A_0 (K_\sigma)^+.$$

This comes from

$$A_0^{-1/2} (A_0 K_\sigma) A_0^{-1/2} = A_0^{1/2} K_\sigma A_0^{-1/2}.$$

Second, we see that the eigenvectors of  $K_\sigma$  are orthogonal for the metric defined by  $A_0$ ,

$$\langle \mathbf{u}, \mathbf{v} \rangle_{A_0} = \mathbf{u}^T A_0 \mathbf{v}$$

Last, we can split  $\mathbb{R}^p$  as  $\mathbb{R}^p = \mathbf{U} \oplus \mathbf{V}$  where  $\mathbf{U}$  is the vector space generated by the vectors that are eigenvectors of  $A_x$  and  $A_y$ , and  $\mathbf{V}$  its orthogonal for the above metric. For the Euler equations,  $\mathbf{U}$  is generated by the eigenvector associated to the transport of entropy.

We see that for any  $\mathbf{x} \in \mathbb{R}^p$ , defining a orthonormal basis of  $\mathbf{U}$  as  $(\mathbf{u}_i)_{i=1, \dots, p}$  and writing  $\mathbf{x} = \sum_{i=1}^p \langle \mathbf{x}, \mathbf{u}_i \rangle \mathbf{u}_i + \mathbf{v}$ , we have

$$K_\sigma^+ \mathbf{x} = \sum_{i=1}^p \lambda_i^+ \langle \mathbf{x}, \mathbf{u}_i \rangle \mathbf{u}_i + K_\sigma^+ \mathbf{v},$$

where  $K_\sigma^+ \mathbf{v} \in \mathbf{V}$ . Hence,

$$\left( \sum_{P, \sigma \in P} K_\sigma^+ \right) \mathbf{x} = \sum_{i=1}^p \left( \sum_P \lambda_i^+ \right) \langle \mathbf{x}, \mathbf{u}_i \rangle \mathbf{u}_i + \sum_P K_\sigma^+ \mathbf{v}.$$

Then we see that  $\sum_{P, \sigma \in P} K_\sigma^+$  is invertible on  $\mathbf{V}$  because for any  $\mathbf{v}$ ,

$$\langle \mathbf{v}, \sum_{P, \sigma \in P} K_\sigma^+ \mathbf{v} \rangle \geq 0$$

and if it were 0 for some  $\mathbf{v} \neq \mathbf{0}$  with  $\mathbf{v} \in V$ , then we would have for all  $\sigma \in P$ ,  $\langle \mathbf{v}, K_\sigma^+ \mathbf{v} \rangle = 0$ . This implies that  $(K_\sigma^+)^{1/2} \mathbf{v} = 0$ , that is  $\mathbf{v} \in \mathbf{V}$  is in the null space of  $(K_\sigma^+)^{1/2}$ . But the null space of  $(K_\sigma^+)^{1/2}$  is that of  $K_\sigma^+$  so that

$$K_\sigma^+ \mathbf{v} = 0,$$

that is  $\mathbf{v} \neq \mathbf{0}$  would be a common eigenvector of all the  $\mathbb{K}_\sigma$ , this is impossible:  $\mathbf{v} = 0$ . This shows that the restriction of  $\sum_{P, \sigma \in P} K_\sigma^+$ , that we still denote by  $\sum_{P, \sigma \in P} K_\sigma^+$  is invertible on  $\mathbf{V}$ .

In the end we get

$$\mathbf{N}_\sigma K_\sigma^+ \mathbf{x} = \sum_{i=1}^p \frac{\lambda_i^+}{\sum_P \lambda_i^+} \langle \mathbf{x}, \mathbf{u}_i \rangle \mathbf{u}_i + \left( \sum_P K_\sigma^+ \right)^{-1} K_\sigma^+ \mathbf{v}.$$

If we consider  $\text{sign}(K_\sigma)$  instead, the proof is the same.